RESEARCH ARTICLE | JUNE 04 2024

Modeling of periodical shearing flow in a fibrous space with applications in shear-induced brain injury $\ensuremath{ \odot}$

Ji Lang 💿 ; Liyun Wang; Qianhong Wu 🗷 💿



Physics of Fluids 36, 061901 (2024)

https://doi.org/10.1063/5.0206943









Modeling of periodical shearing flow in a fibrous space with applications in shear-induced brain injury

Cite as: Phys. Fluids **36**, 061901 (2024); doi: 10.1063/5.0206943 Submitted: 5 March 2024 · Accepted: 11 May 2024 · Published Online: 4 June 2024







Ji Lang,^{1,2} 🕞 Liyun Wang,³ and Qianhong Wu^{4,5,a)} 🕞



AFFILIATIONS

- ¹School of Mechanical Engineering, Southeast University, Nanjing 211189, China
- 2 Jiangsu Key Laboratory for Design and Manufacture of Micro-Nano Biomedical Instruments, School of Mechanical Engineering, Southeast University, Nanjing 211189, China
- ³Department of Mechanical Engineering, University of Delaware, Newark, Delaware 19716, USA
- 4 Cellular Biomechanics and Sports Science Laboratory at Villanova University, 800 E Lancaster Avenue, Villanova, Pennsylvania 19085, USA
- ⁵Department of Mechanical Engineering, Villanova University, 800 E Lancaster Avenue, Villanova, Pennsylvania 19085, USA

ABSTRACT

This paper presents a theoretical model examining the interaction between a fibrous network and viscous fluid flow driven by an oscillating boundary. The aim is to understand how oscillating impacts are transmitted from the skull, through the arachnoid trabeculae network filled with cerebrospinal fluid, as observed in shaken baby syndrome. The model uses an effective medium approach to determine the fluid velocity field while each fiber is treated as a soft string undergoing deformation. Results indicate that the frequency of oscillation, fiber stiffness, and porous structure resistance significantly influence the oscillating shearing flow, as indicated by the Womersley (Wo), Brinkman (a), and Bingham (Bm) numbers. Application of the model to shaken baby syndrome suggests that oscillations in the cerebrospinal fluid and arachnoid trabeculae can significantly surpass those on the skull, leading to intense shear stress penetration to the brain. This model is the first study to integrate the dynamic response of string-like fibrous networks in fluid flows with oscillating boundaries and offers a quantitative framework for predicting the transmission of shearing forces from the skull to the brain matter.

Published under an exclusive license by AIP Publishing. https://doi.org/10.1063/5.0206943

I. INTRODUCTION

Shearing flow through a fibrous network involves the interactions and deformations of flexible fibers with fluid flow. It is widely observed in industrial applications and biological systems. 1-3 Some examples include microorganismal swimming, nuclear positioning in eukaryotic cells,5 and the motion of red cells over the endothelial glycocalyx layer that covers the inner surface of blood vessels.⁶⁻⁹ The present paper is inspired by our recent study about brain injury due to rotational impacts on the head. The brain is the main organ in the human central nervous system. Figure 1(a) shows the basic structure of the head, where the soft brain tissue is enclosed in the hard skull. Between them, there is a thin subarachnoid space (SAS), which is filled with cerebrospinal fluid (CSF) derived from blood plasma.³ The gap of the SAS is typically below 3 mm in thickness and contains thin connective tissue strands called arachnoid trabeculae (AT) that loosely connect the inner surface of the skull and the outer surface of the brain matter. 10-13 Figure 1(b) shows the detailed structure of the SAS where one end of the AT is attached to the Pia matter that covers the outer surface of the brain, while the other end of it is attached to the arachnoid membrane that lines the inner side of the skull. With a radius of $r = 15 \,\mu\text{m}$, AT is too thin to be detected by ultrasound or highresolution magnetic resonance imaging (MRI). However, in recent years, it has been studied extensively with the aid of transmission electron microscopy and scanning electron microscopy. 14,15 Despite their thin profile, AT serve to suspend the brain within the CSF-filled SAS and severely restrict relative motion between the skull and brain surface. 16 Due to its existence, the SAS is considered to be a porous space¹⁷ whose permeability is estimated to be $3.125 \times 10^{-10} \,\mathrm{m}^2$. ¹⁶

^{a)}Author to whom correspondences should be addressed: qianhong.wu@villanova.edu

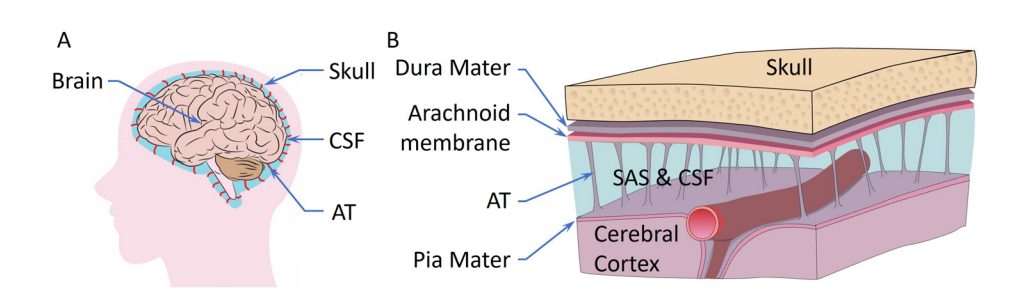


FIG. 1. (a) Basic structure of the head and (b) Sketch of the subarachnoid space. Fibrous arachnoid trabeculae connect the arachnoid membrane and pia mater across the gap.

When a sudden impact is imposed on the head, some critical and fundamentally important questions one would ask are the following: How is an impact on the skull transmitted through the SAS to the soft brain matter? What is the role of the CSF flow through the porous AT network during the force transmission process? To answer these questions, one must thoroughly understand the fluid-structure interaction between the CSF and AT during the impact process.

Impacts on the head are commonly identified as the cause of brain injury. 18,19 Repetitive head impacts, even those with no acute symptoms or signs, have been suggested as a possible cause of chronic brain injury (CBI).²⁰ For example, shaken baby syndrome is the most common cause of neurological injury in children.^{21,22} When a baby is shaken periodically, the skull is forced to move concurrently. As a result, the AT would be dragged to move and deform, 23 and the CSF would flow simultaneously. It is expected that the viscous flow of the CSF through the AT porous network plays a critical role in mitigating the impact by acting as a damping system. It also behaves as a bridge to transmit the shearing impact from the skull to the soft brain matter. Therefore, the dynamics of fluid-structure interaction between the fibrous network and viscous fluid flow, driven by an oscillating boundary, are central to understanding the physics of force transmission. Exploring this mechanism offers insights into physiological or pathological processes like those observed in shaken baby syndrome.

The viscous shearing flow driven by a tangentially moving boundary could date back to Couette flow. Since then, extensive studies have been developed to investigate all flow phenomena caused by the tangentially moving boundary. For example, a series of studies investigated the flow instability and transition caused by the oscillating boundary. The shearing flow patterns formed during the Taylor-Couette flow have drawn wide attention. Phenomena like nanoferroliquid flow and droplet deformation under parallel shearing flow have also been studied.

When a space is filled with fibrous porous media, the mechanism of the fluid flowing through and its interaction with the fibrous structure becomes important. Both anchored and freely suspended flexible fibers have recently been studied. The fibers are either actuated or passively driven by the fluid flow. Luhar and Nepf³¹ investigated waveinduced oscillatory flow through natural aquatic vegetation, and the wave energy dissipation caused by the flexible blades was discussed. Elastic fibers like flagella and cilia deformed in a shear flow have been studied by Zuk *et al.*³² and Becker and Shelley.³³ Fiber bending, curling, and rotation caused by the flow have been solved.

Theoretically, the interaction between flexible fibers and viscous fluids has been extensively researched using two main approaches. The local slender body theory (SBT) employs the Stokes equation to analyze fluid flow around individual fibers, providing a local relation

between elastic and drag forces.³⁴ Conversely, the effective medium approach examines the global interaction of a fibrous network with viscous flow, utilizing the Brinkman equation. In this method, fibers are often modeled as cantilever beams undergoing small³⁴ and large deformations,^{31,35} or as a series of beads.^{32,36} However, the cantilever beam or beads model is inappropriate for applications involving very soft, string-like fibers observed in biological systems, e.g., AT. Hence, a notable research gap is evident in the theoretical modeling of fiber behavior, especially in systems closely resembling physiological environments.

In this paper, we have developed a unique theoretical model that explores the interaction between a fibrous network and a viscous fluid flow. A string function describes the fiber displacement, while an effective medium approach governs the fluid flow through the fiber. 37–43 A comprehensive parametric study will be performed to examine primary factors that govern the fluid-structure interaction process. Finally, we will apply the model to examine the CSF flow in the SAS through the fibrous AT network. This model is among the first to integrate the dynamic response of fibrous networks in fluid flows with oscillating boundaries, offering a new perspective to examine these complex interactions. Our application of the developed theory to estimate the interaction between the AT and CSF flow under mechanical impacts provides the first quantitative framework to predict the transmission of shearing forces from the skull to the brain matter.

II. THEORETICAL MODEL

Figure 2(a) shows a simplified SAS. Evenly distributed fibers extend across the liquid gap, with their two ends anchored to the fixed bottom and the horizontally oscillating top plate. The fiber network has been assumed to be homogeneous. The coordinate system (y) and the gap height (h) are shown in Fig. 2(a). The fibers and the fluid will be driven by the top plate and interact with each other. Figure 2(b) shows the forces acting on a single fiber element, which includes the tension force, T, along the fiber and the fluid drag force, F_l , in the horizontal direction. ξ in the figure represents the horizontal displacement of the fiber. This problem features a thin gap height, a fibrous structure, and a horizontally oscillating boundary. It is assumed that the velocity of the top plate follows a sine function, $V_0 \sin(\omega t)$, where V_0 is the characteristic velocity, ω is the angular frequency, and t is time.

Darcy-Lapwood-Brinkman model, ^{44–46} which accounts for the inertial effect, the viscous effect, and the hydraulic resistance from the porous media, is used in this study to capture the fluid flow,

$$\rho \left[\frac{\partial \mathbf{u}}{\partial t} + (\mathbf{u} \cdot \nabla) \mathbf{u} \right] = -\nabla P + \mu \nabla^2 \mathbf{u} - \frac{\mu}{K_p} \mathbf{u}. \tag{1}$$

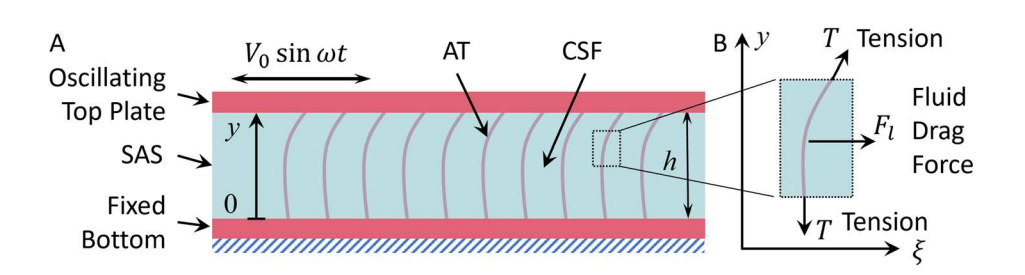


FIG. 2. Sketch of the problem. (a) Simplified SAS featuring evenly distributed fibrous AT within the CSF. (b) The free-body diagram of a fiber element.

where $\mathbf{u} = \phi \mathbf{u}'$ is the local macroscopic velocity of the fluid, ϕ is the porosity defined as the fraction of the total volume that is occupied by void spaces within a material, \mathbf{u}' is the microscopic velocity of the fluid, ρ is the fluid density, P is the pressure, μ is the dynamic viscosity of the fluid, and K_p is the Darcy permeability. Here, as the gap is very thin, the gravitational force is neglected.

Considering the gap height is significantly smaller than the length scale of the flow channel in the flow direction, we assume the flow within the gap to be unidirectional. Then, Eq. (1) is simplified as

$$\rho \frac{\partial u}{\partial t} = \mu \frac{\partial^2 u}{\partial y^2} - \frac{\mu}{K_p} u, \tag{2}$$

where u is the horizontal component of the local macroscopic velocity. $u = \phi u'$, where u' is the horizontal component of the microscopic velocity.

The last term in Eq. (2) represents the hydraulic resistance caused by the relative motion between the fluid and the porous structure. As the fibers can also move and deform, the last term in Eq. (2) has been modified based on a relative velocity,

$$\rho \frac{\partial u}{\partial t} = \mu \frac{\partial^2 u}{\partial y^2} - \frac{\mu}{K_p} \left(u - \phi \frac{\partial \xi}{\partial t} \right). \tag{3}$$

We assume the fiber displacement in the vertical direction is negligible compared to the displacement in the horizontal direction. Hence, the fiber is treated as a string. According to the force analysis shown in Fig. 2(b), the governing equation of a single fiber is

$$\rho_s \pi R_f^2 \frac{\partial^2 \xi}{\partial t^2} = T \frac{\partial^2 \xi}{\partial y^2} + \frac{\pi R_f^2}{1 - \phi} \frac{\mu}{K_p} \left(u - \phi \frac{\partial \xi}{\partial t} \right), \tag{4}$$

where ρ_s is the density of the fiber, R_f is the fiber radius. The term on the left-hand side (LHS) represents the acceleration; the first term on the right-hand side (RHS) represents the tension force from the stretched fiber; the second term on the RHS is the flow resistance force received by a single fiber, which is the reaction force of the last term in Eq. (3). Here, it is assumed that the tension force, T, is the average force along the fiber and does not change with time. This assumption is based on the linear deformation theory, suggesting minimal tension variations in the scenarios we modeled. This simplification enables an analytical solution, providing a foundational understanding of the fluid-solid interactions with minimal impact on the accuracy of the phenomena being studied. The term $\pi R_f^2/(1-\phi)$ represents the effective cross-sectional area of an infinitesimal fiber element within a porous medium, adjusted for the fiber's volume fraction in that medium. Then, the last term on the RHS captures the force received by the fiber, which effectively is the reaction force of the porous resistance. The fluid starts from a static state, and the fiber has no displacement and zero velocity:

$$u = 0, \ \xi = 0, \quad \text{and} \quad \frac{\partial \xi}{\partial t} = 0, \quad \text{when } t = 0.$$
 (5)

The boundary conditions at the fixed bottom, where y = 0, are

$$u = 0$$
 and $\xi = 0$. (6)

The oscillating boundary conditions at the top plane, where y = h, are

$$u = \phi V_0 \sin(\omega t)$$
 and $\frac{\partial \xi}{\partial t} = V_0 \sin(\omega t)$. (7)

Here, the following dimensionless numbers are defined: $y^* = y/h$, $u^* = u/(\phi V_0)$, $\xi^* = \xi/(V_0/\omega)$, $t^* = t/t_0$, $t_0 = 1/\omega$, and Brinkman number, $t_0 = 1/\omega$, t_0

The Bingham number (Bm) measures the balance between fiber tension and viscous forces, illustrating the role of fiber stiffness in fluid–structure interactions; a higher Bm suggests increased fiber stiffness. The Womersley number (Wo) compares inertial to viscous forces, which are vital for analyzing fluid behavior under oscillatory conditions; a greater Wo signifies more pronounced oscillatory effects. The Brinkman number (α) evaluates the porous medium's permeability, indicating the porous resistance relative to viscous forces; a higher α reflects a stronger porous resistance.

Equations (3) and (4) can then be cast into a dimensionless format,

$$Wo^{2} \frac{\partial u^{*}}{\partial t} = \frac{\partial^{2} u^{*}}{\partial v^{*2}} - \alpha^{2} u^{*} + \alpha^{2} \frac{\partial \xi^{*}}{\partial t^{*}}, \tag{8}$$

$$Wo^{2}\eta \frac{\partial^{2} \xi^{*}}{\partial t^{*2}} + \frac{\phi \alpha^{2}}{1 - \phi} \frac{\partial \xi^{*}}{\partial t^{*}} = Bm \frac{\partial^{2} \xi^{*}}{\partial y^{*2}} + \frac{\phi \alpha^{2}}{1 - \phi} u^{*}.$$
 (9)

The dimensionless initial condition is given by

$$u^* = 0, \ \xi^* = 0, \quad \text{and} \quad \frac{\partial \xi^*}{\partial t^*} = 0 \quad \text{when } t^* = 0,$$
 (10)

and the dimensionless boundary conditions become

$$u^* = 0$$
 and $\xi^* = 0$ at $y^* = 0$, (11)

as well as

$$u^* = \sin(t^*)$$
 and $\frac{\partial \xi^*}{\partial t^*} = \sin(t^*)$ at $y^* = 1$. (12)

Laplace transform is performed on Eqs. (8) and (9),

$$\frac{\partial^2 \bar{u}}{\partial y^{*2}} - (Wo^2 s + \alpha^2) \bar{u} + \alpha^2 s \bar{\xi} = 0, \tag{13}$$

$$\bar{u} = -\frac{1-\phi}{\phi\alpha^2} \operatorname{Bm} \frac{\partial^2 \bar{\xi}}{\partial y^{*2}} + \left(\frac{1-\phi}{\phi\alpha^2} \operatorname{Wo}^2 \eta s^2 + s\right) \bar{\xi}, \qquad (14)$$

where \bar{u} and $\bar{\xi}$ are the Laplace transform of u^* and ξ^* , and s is the Laplace operator.

The transformed boundary conditions become

$$\bar{u} = 0$$
 and $\bar{\xi} = 0$ at $y^* = 0$, (15)

and

$$\bar{u} = \frac{1}{s^2 + 1}$$
 and $\bar{\xi} = \frac{1}{s(s^2 + 1)}$ at $y^* = 1$. (16)

Substituting Eq. (14) into Eq. (13), the governing equation could be simplified as an ordinary differential equation of ξ ,

$$\frac{\partial^4 \bar{\xi}}{\partial v^{*4}} - \beta_1 \frac{\partial^2 \bar{\xi}}{\partial v^{*2}} + \beta_2 \bar{\xi} = 0, \tag{17}$$

where

$$\beta_{1} = s^{2} \frac{\mathrm{Wo}^{2} \eta}{\mathrm{Bm}} + s \left(\mathrm{Wo}^{2} + \frac{1}{\mathrm{Bm}} \frac{\alpha^{2} \phi}{1 - \phi} \right) + \alpha^{2},$$

$$\beta_{2} = s^{3} \frac{\mathrm{Wo}^{4} \eta}{\mathrm{Bm}} + s^{2} \frac{\mathrm{Wo}^{2} \alpha^{2}}{\mathrm{Bm}} \left(\frac{\phi}{1 - \phi} + \eta \right).$$
(18)

Substituting Eqs. (15) and (16) into Eq. (14), the fluid boundary conditions could be transferred to the boundary conditions of the solid fiber,

$$\bar{\xi} = 0$$
 and $\frac{\partial^2 \bar{\xi}}{\partial y^{*2}} = 0$, at $y^* = 0$, (19)

and

$$\bar{\xi} = \frac{1}{s(s^2 + 1)}$$
 and $\frac{\partial^2 \bar{\xi}}{\partial y^{*2}} = \frac{Wo^2 \eta}{Bm} \frac{s}{s^2 + 1}$ at $y^* = 1$. (20)

Subject to the boundary conditions, Eqs. (19) and (20), Eq. (17) is solved analytically, which gives

$$\bar{\xi} = \frac{\left(\lambda_2^2 - \frac{\mathrm{Wo}^2 \eta}{Bm} s^2\right)}{s(s^2 + 1)\left(\lambda_2^2 - \lambda_1^2\right)} \frac{\sinh(\lambda_1 y)}{\sinh(\lambda_1)} - \frac{\left(\lambda_1^2 - \frac{\mathrm{Wo}^2 \eta}{Bm} s^2\right)}{s(s^2 + 1)\left(\lambda_2^2 - \lambda_1^2\right)} \frac{\sinh(\lambda_2 y)}{\sinh(\lambda_2)},$$
(21)

where

$$\lambda_1 = \sqrt{\frac{\beta_1 + \sqrt{{\beta_1}^2 - 4\beta_2}}{2}}$$
 and $\lambda_2 = \sqrt{\frac{{\beta_1 - \sqrt{{\beta_1}^2 - 4\beta_2}}}{2}}$. (22)

Substituting Eq. (21) into Eq. (14), one obtains the solution of the fluid flow,

$$\bar{u} = \left(Wo^{2}\eta \frac{1-\phi}{\alpha^{2}\phi}s^{2} + s\right) \left[\frac{\left(\lambda_{2}^{2} - \frac{Wo^{2}\eta}{Bm}s^{2}\right)}{s(s^{2}+1)\left(\lambda_{2}^{2} - \lambda_{1}^{2}\right)} \frac{\sinh(\lambda_{1}y)}{\sinh(\lambda_{1})} - \frac{\left(\lambda_{1}^{2} - \frac{Wo^{2}\eta}{Bm}s^{2}\right)}{s(s^{2}+1)\left(\lambda_{2}^{2} - \lambda_{1}^{2}\right)} \frac{\sinh(\lambda_{2}y)}{\sinh(\lambda_{2})} \right] - \frac{1-\phi}{\alpha^{2}\phi} \operatorname{Bm} \left[\frac{\lambda_{1}^{2}\left(\lambda_{2}^{2} - \frac{Wo^{2}\eta}{Bm}s^{2}\right)}{s(s^{2}+1)\left(\lambda_{2}^{2} - \lambda_{1}^{2}\right)} \frac{\sinh(\lambda_{1}y)}{\sinh(\lambda_{1})} - \frac{\lambda_{2}^{2}\left(\lambda_{1}^{2} - \frac{Wo^{2}\eta}{Bm}s^{2}\right)}{s(s^{2}+1)\left(\lambda_{2}^{2} - \lambda_{1}^{2}\right)} \frac{\sinh(\lambda_{2}y)}{\sinh(\lambda_{2})} \right].$$

$$(23)$$

Applying the Euler Algorithm⁴⁷ to inverse Laplace transform Eq. (21) and Eq. (22), f^* and u^* are obtained as

$$\xi^*(t^*, y^*) = \frac{10^{M/3}}{t^*} \sum\nolimits_{k=0}^{2M} \delta_k \Re\left\{ \bar{\xi} \left(s = \frac{\gamma_k}{t^*}, y^* \right) \right\}, \quad (24)$$

$$u^*(t^*, y^*) = \frac{10^{M/3}}{t^*} \sum\nolimits_{k=0}^{2M} \delta_k \Re\left\{ \bar{u}\left(s = \frac{\gamma_k}{t^*}, y^*\right) \right\}, \quad (25)$$

where

$$\gamma_k = \frac{M\ln(10)}{3} + \pi i k \quad \text{and} \quad \delta_k = (-1)^k \zeta_k. \tag{26}$$

Here, $\bar{\xi}$ and \bar{u} are complex numbers, $i=\sqrt{-1}$, M is an integer indicating the number of terms in the approximation, and \Re denotes the real part of the complex number in the curly braces. ζ_k satisfies

$$\zeta_0 = \frac{1}{2}, \quad \zeta_{2M} = \frac{1}{2^M}, \quad \zeta_k = 1, \quad 1 \le k \le M,$$
 (27)

and

$$\zeta_{2M-k} = \zeta_{2M-k+1} + 2^{-M} \binom{M}{k}, \quad 0 < k < M.$$
(28)

After examination, the difference between the solutions with M=10, and M=15 are negligible, and hence, in the following section, M=10 is used to plot the results.

With the solved fluid velocity and the fiber displacement, one can find the shear stress,

$$\tau = \mu \frac{\partial u}{\partial y}$$
 and $\tau^* = \frac{\partial u^*}{\partial y^*}$, (29)

where τ and τ^* are dimensional and dimensionless shear stress, respectively, related by $\tau = \phi \mu \frac{V_0}{l_*} \tau^*$.

The porous resistance received by the fluid, as a body force, is solved as

$$b = -\frac{\nu}{k_p} \left(u - \frac{\partial \xi}{\partial t} \right) \quad \text{and} \quad b^* = \frac{\partial \xi^*}{\partial t^*} - u^*, \tag{30}$$

where b and b^* are dimensional and dimensionless porous resistance, respectively, related by $b=\phi V_0 \frac{\nu}{k_p} b^*$. A positive b^* means the fiber moves faster than the fluid in the positive direction.

The theoretical model developed here marks a step forward in comprehending fluid-structure interactions within environments like SAS, offering an analytical framework for examining these dynamics with practical implications. It enriches our understanding of how fibrous networks interact with fluid flows, positioning the model as a powerful instrument for simulating physiological scenarios. Nonetheless, it should be recognized that the model relies on assumptions of unidirectional flow and linear fiber deformations, although simplifying the analytical process may restrict its precision in instances involving considerable gap heights or pronounced fiber deformation.

The linear fiber deformation assumption simplifies the complex interactions within the SAS by treating Young's modulus of the fibers as constant, thus not accounting for any non-linear behavior or changes in material properties under different stress states. Additionally, we assume that the fibers are structurally robust enough to withstand mechanical stresses without breaking or undergoing any form of structural failure within the tested deformation limits. These assumptions are based on the limited availability of comprehensive data on the mechanical properties of AT and are used to derive manageable and analytical solutions within the scope of this study. Further investigations are needed to validate these assumptions and expand the model to include non-linear dynamics and failure mechanisms as more detailed mechanical property data becomes available.

III. RESULTS AND DISCUSSION

This section will present the theoretically predicted fluid velocity, fiber displacement, shear stress distribution, and porous resistance distribution. As shown in Eqs. (21) and (23), the problem is governed by the oscillating frequency (Wo), the stiffness of the fiber (Bm), and the permeability of the porous domain (α). As the density difference between the fluid and the solid tissue is negligible in the biological system, $\eta=1$ is used in this study. In addition, $\phi=0.99$ is used as a representative porosity in the space. A parametric study will be performed to investigate the influence of Wo, Bm, and α . Then, an application to the actual biological system will be calculated and discussed.

In the parametric study, the selection of parameters for Bm, Wo, and α were carefully chosen to illuminate how the model responds under different conditions related to fiber stiffness, the frequency of oscillatory loading, and the porosity of the media. The focus extended beyond merely duplicating conditions associated with rotational head injuries, striving instead to clarify the underlying dynamics governed by these parameters. This strategy highlighted the model's adaptability and its broad potential for application to a variety of challenges, laying a groundwork for more specific future research.

In the results, the fluid velocity, u^* , and the fiber displacement, f^* , which directly reveals the fluid flow behavior and the fiber displacement, will be presented first. Then, the shear stress distribution, τ^* , calculated by Eq. (29), revealing how the boundary oscillation penetrates the gap, will be plotted. $\tau^*=1$ equals the shear stress from a Couette flow. At last, we will present the porous resistance distribution, b^* , which is solved by Eq. (30). A positive b^* means the fiber moves faster than the fluid, while a negative value indicates a faster fluid than the fiber.

A. Parametric study on oscillating frequency

Figures 3–5 show a parametric study of the fluid flow, fiber displacement, fluid shear stress, and porous resistance with different frequencies. The parameters are Bm = 1, α = 1, for different values of Wo numbers (1, 5, and 10).

Figure 3 shows the results of the fluid flow and fiber displacement. Figure 3(a) illustrates a representative result of fluid flow across the gap with a low frequency (Wo = 1). It includes four subplots, in which the horizontal coordinate, u^* , represents the fluid velocity and the vertical coordinate, z^* , is the vertical position. Each subplot includes 11 radial velocity profiles. The dimensionless time step between two consecutive profiles is $\pi/20$, 1/40 of an oscillating period. Therefore, one subplot tracks the fluid velocity change during a quarter of the oscillating boundary period. The starting and ending times of each subplot are shown in the figure, and the profiles' color changes from green to red, indicating the forward time direction. The results for higher oscillating frequencies are presented in Figs. 3(b) (Wo = 5) and 3(c) (Wo = 10). Figure 3(d) illustrates the fiber displacement across the gap at the same working condition as that of Fig. 3(a). Figure 3(d) includes two subplots in which the horizontal coordinate, ξ^* , represents the fiber displacement and the vertical coordinate, y^* , is the vertical position. Each subplot includes 21 radial velocity profiles. The dimensionless time step between two consecutive profiles is $\pi/40$, 1/80 of an oscillating period. Therefore, one subplot follows the fluid velocity change during a half boundary oscillating period. The color of profiles in each subplot changes from blue to orange, indicating the forward time direction. Similarly, for higher frequencies, the fiber displacement is shown in Figs. 3(e) (Wo = 5) and 3(f) (Wo = 10).

Figure 3 indicates that when the frequency is small, as shown in Figs. 3(a) and 3(d), the viscous effect would be dominant, and hence, the fluid velocity and the fiber displacement have a linear shape. In this condition, the flow behavior is like the classical Couette flow. As the frequency increases, the inertia effect becomes more significant. The results illustrated in Figs. 3(b), 3(c), 3(e), and 3(f) show that both the fluid velocity and the fiber displacement begin to fluctuate. The depth influenced by the oscillating boundary decreases, which means the fluid and the fiber at the bottom would have a weaker response when the frequency is higher. Overall, the fluid and fibers in the gap are strongly coupled, making the behavior highly sensitive to the oscillation frequency.

Figure 4 shows the results of the shear stress, τ^* , across the gap with different frequencies. Figure 4(a) shows a representative result of the shear stress distribution at a low frequency (Wo = 1). Figure 4(a) includes four subplots and has 11 radial shear stress profiles in each subplot. Similar to Fig. 3(a), one subplot consists of the shear stress change during a quarter of a boundary oscillation period. The starting and ending times of each subplot are shown in the figure, and the color of the profiles changes from green to red, indicating the forward time direction.

Figure 4(a) indicates that, with a low frequency, the shear stress would have an even distribution across the gap, which means the viscous effect is dominant and the boundary oscillation has enough time to penetrate to the bottom. As the frequency increases, the magnitude of the shear stress increases, but the penetration depth of the shear stress caused by the oscillating boundary quickly decreases, which is shown in Figs. 4(b) (Wo = 5) and 4(c) (Wo = 10). The reason is that the fast-changing boundary motion in one period could counterbalance itself.

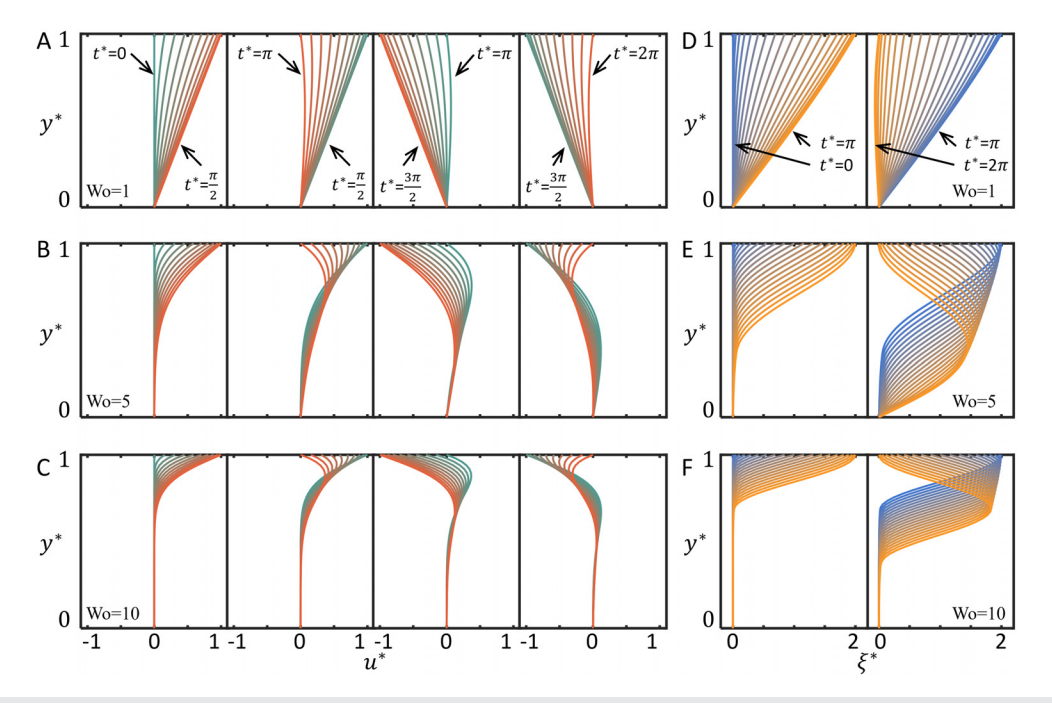


FIG. 3. (a)–(c) Fluid velocity and (d)–(f) fiber displacement profile across the gap with parameters Bm=1, $\alpha=1$, and different frequencies (Wo₀ = 1, 5, 10). Each of (a)–(c) shows four subplots of the fluid velocities during one-quarter of a period. Each of (d)–(f) shows two subplots of the fiber displacements during one-half of a period. The starting and ending times of each subplot are shown in (a) and (d). As the frequency increases, both profiles change from a linear shape to an oscillating profile, and the penetration depth influenced by the oscillating top plate decreases.

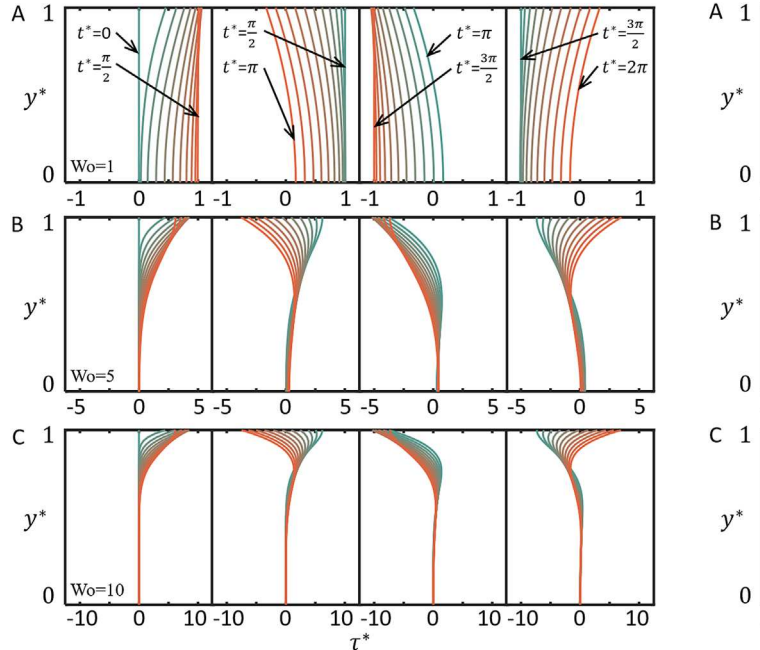


FIG. 4. (a)–(c) Fluid shear stress profile across the gap with parameters Bm = 1, α = 1, and different frequencies (Wo₀ = 1, 5, 10). Each of (a)–(c) shows four subplots of shear stress during one-quarter of a period. The starting and ending times of each subplot are shown in (a). For higher frequencies, the shear stress increases while the penetration depth decreases.

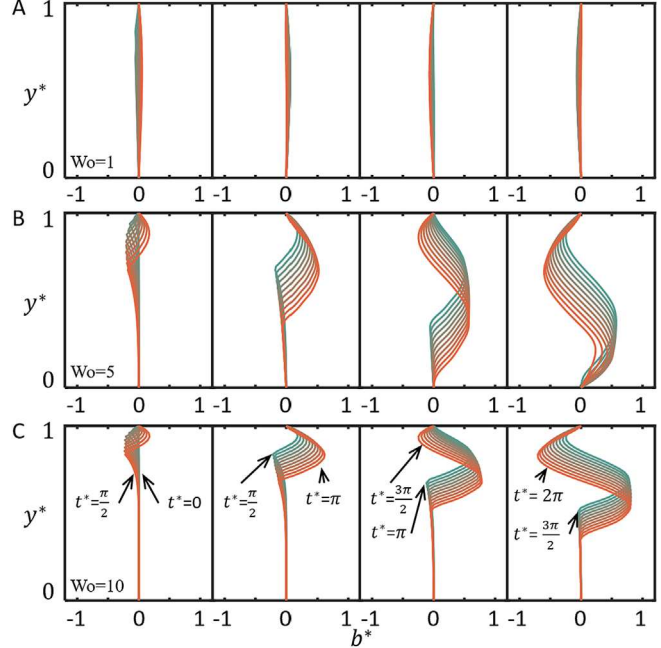


FIG. 5. (a)–(c) Porous resistance profile across the gap with parameters Bm = 1, α = 1, and different frequencies (Wo₀ = 1, 5, 10). Each of (a)–(c) shows four subplots of the porous resistance during one-quarter of a period. The starting and ending times of each subplot are shown in (c). With increasing frequency and as time progresses, the porous resistance increases.

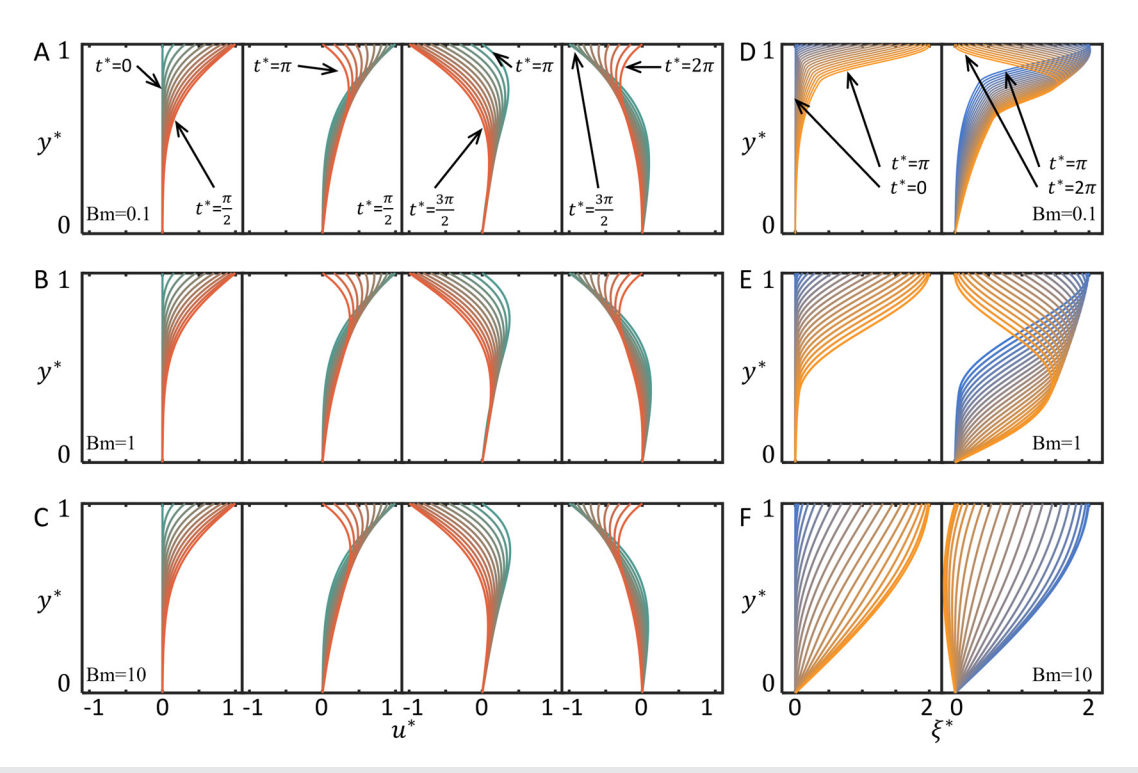


FIG. 6. (a)–(c) Fluid velocity and (d)–(f) fiber displacement profile across the gap with parameters Wo = 5, $\alpha = 1$, and different values of fiber stiffness (Bm = 0.1, 1, 10). As the fiber stiffness increases, the fiber displacement becomes more linear, with little influence on the fluid velocity.

Figure 5 shows the results of the porous resistance across the gap with different frequencies. Each of Figs. 5(a)–5(c) includes four subplots, each of which has 11 radial shear stress profiles. Like Fig. 3(a), one subplot consists of the porous resistance change during a quarter boundary oscillating period. The starting and ending times of each subplot are shown in Fig. 5(c), and the color of the profiles changes from green to red, indicating the forward time direction.

Figure 5(a) indicates that, with a low frequency (Wo = 1), the porous resistance is negligible, which means the fluid and the fiber would move without much difference in velocity. With an increasing frequency, as the results shown in Figs. 5(b) (Wo = 5) and 5(c) (Wo = 10), the velocity difference begins to increase. At the starting moment, the fluid responds faster, and later, the fibers move faster. The higher frequency would decrease the influence penetration depth within the first period because the wave speed along the fiber is independent of the frequency. Therefore, the case with higher frequency would have less time to transmit the influence into the gap.

B. Parametric study on fiber stiffness

Figures 6–8 show a parametric study of the fluid flow, fiber displacement, fluid shear stress, and porous resistance with different fiber stiffness. The parameters are Wo = 5, α = 1, and different Bm numbers (0.1, 1, and 10). A larger Bm corresponds to a stiffer fiber.

Figure 6 shows the results of the fluid flow and fiber displacement for different values of fiber stiffness. Similar to Fig. 3, Figs. 6(a)–6(c) show the fluid velocity and Figs. 6(d)–6(f) present the fiber

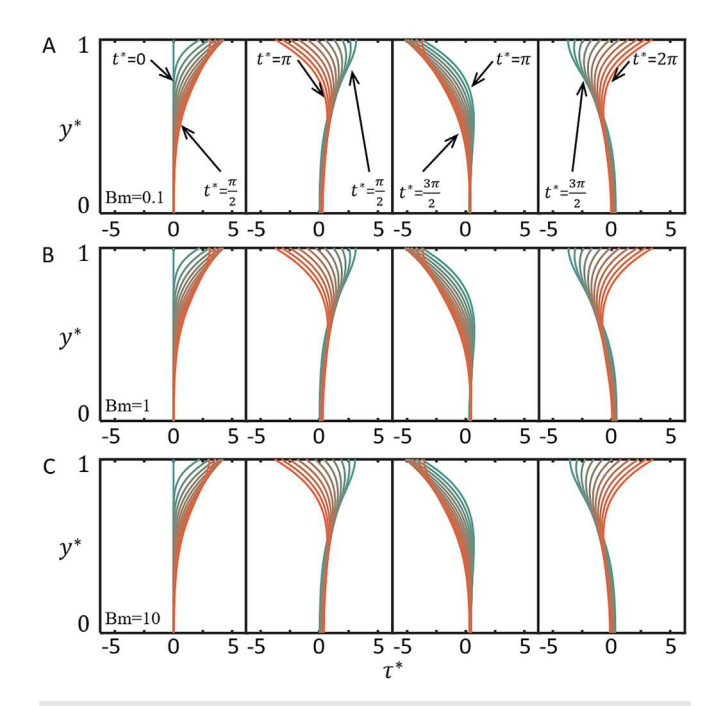


FIG. 7. (a)–(c) Shear stress profile across the gap with parameters Wo = 5, α = 1, and different fiber stiffness (Bm = 0.1, 1, 10). As the fiber stiffness increases, the shear stress experiences limited influence.

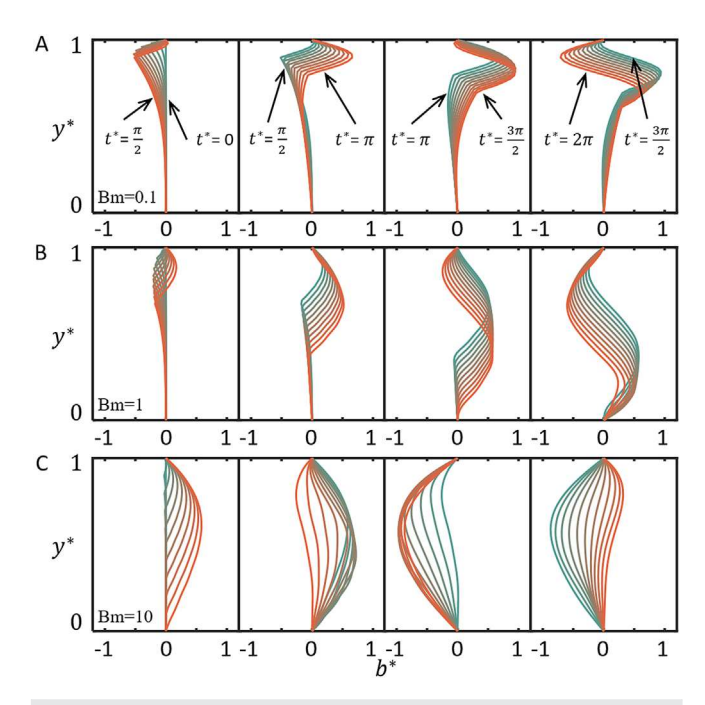


FIG. 8. (a)–(c) Porous resistance profile across the gap with parameters Wo = 5, α = 1, and different fiber stiffness (Bm = 0.1, 1, 10). For a higher fiber stiffness, the propagation speed of the oscillation increases.

displacement. The results indicate that with higher stiffness, the fiber tends to assume a linear profile, as shown in Fig. 6(f). When the fibers become softer, they begin to oscillate, and the displacement near the bottom decreases, as shown in Figs. 6(d) and 6(e). On the other hand, the fluid velocity exhibits limited sensitivity to the fiber stiffness. The reason is that fibers still follow the boundary motion, and hence, the velocity difference between the fluid and the solid is insignificant.

Figure 7 shows the calculated shear stress with different fiber stiffness. Similar to the phenomenon observed in Fig. 6, the results indicate that the fiber stiffness has little influence on the shear stress distribution in the gap.

Figure 8 shows the results of the porous resistance for different fiber stiffnesses. Similar to Fig. 5, Figs. 8(a)–8(c) present the porous resistance in the same way. The results indicate that with higher stiffness (higher Bm), the influence from the top oscillating boundary would penetrate to the bottom within a shorter time. The magnitude of the porous resistance is not much different across these three working conditions.

C. Parametric study on porous resistance

Figures 9–11 show a parametric study of the fluid flow, fiber displacement, fluid shear stress, and porous resistance with different porous permeabilities. The parameters are Wo = 5, Bm = 1, and different α numbers (0.1, 1, and 10). A larger value of α indicates a higher flow resistance from the fibers.

Figure 9 shows the results of the fluid flow and fiber displacement for different porous permeabilities, which is solved for Wo=5,

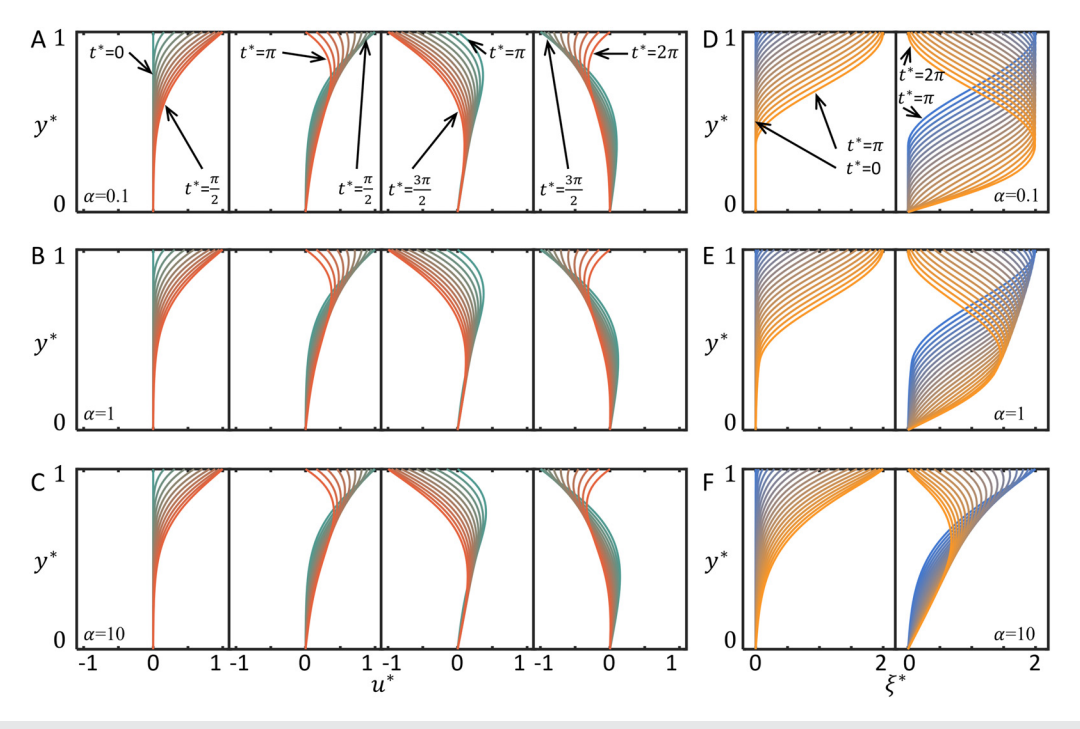


FIG. 9. (a)–(c) Fluid velocity and (d)–(f) fiber displacement profile across the gap with parameters Wo = 5, Bm = 1, and different values of porous resistance ($\alpha = 0.1, 1, 10$). With increasing porous resistance, the fluid velocity has received limited influence, while for the fiber displacements, the oscillation in the bottom region decreases.

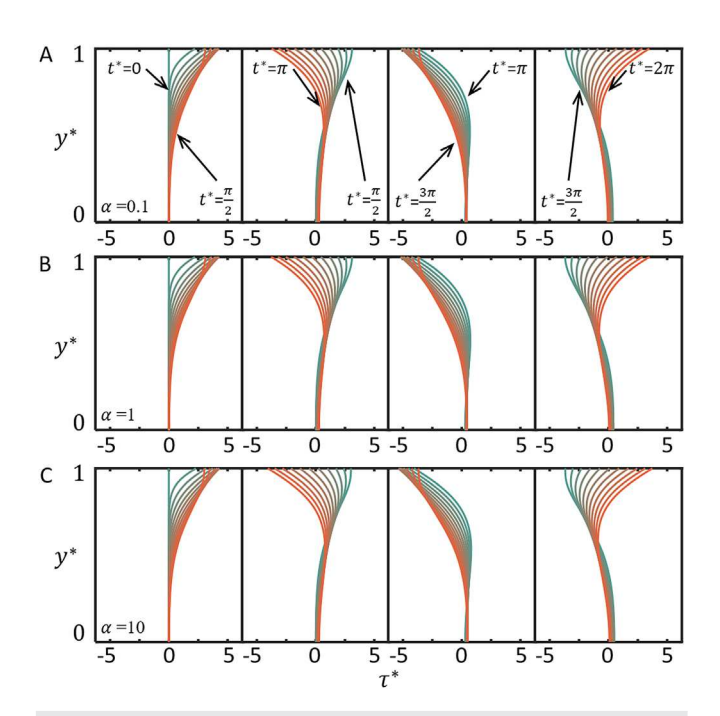


FIG. 10. (a)–(c) Shear stress profile across the gap with parameters Wo = 5, Bm = 1, and different porous resistance (α = 0.1, 1, 10) of the porous resistance, has limited influence on the shear stress.

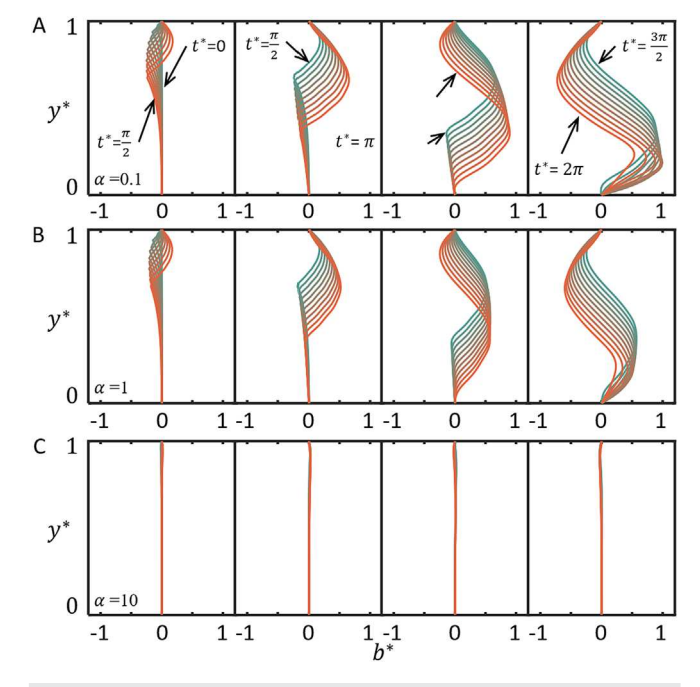


FIG. 11. (a)–(c) Porous resistance profile across the gap with parameters Wo = 5, Bm = 1, and different porous resistance (α = 0.1, 1, 10). For a higher porous resistance, the velocity difference between the fluid and the fiber decreases.

Bm = 1, and different α numbers (0.1, 1, and 10). Similar to Fig. 3, Figs. 9(a)–9(c) present the fluid velocity and Figs. 9(d)–9(f) show the corresponding fiber displacement. The results in Figs. 9(d)–9(f) indicate that the fiber oscillation at the bottom tends to become limited with higher resistance because the higher resistance dissipates the momentum. However, the fluid velocity has undergone little influence from the porous resistance. According to Eq. (9), when α is significant, the velocity difference between the fluid and the fiber becomes negligible ($u^* \approx \frac{\partial \mathcal{E}^*}{\partial t^*}$). Then, it follows from Eq. (8) that the fluid flow becomes independent of α . Therefore, a dense porous fiber structure will not change the fluid flow in the space.

Figure 10 shows the calculated porous resistance. The results indicate that the porous resistance has little influence on the shear stress distribution in the gap.

Figure 11 shows the results of the porous resistance with different porous permeability values. The results in Figs. 11(a)-11(c) indicate that with a higher resistance, the magnitude of the porous resistance decreases. As α reaches 10, the porous resistance becomes negligible, which means the fiber and the fluid move together with no velocity difference.

D. Application to rotational impact-induce brain injury

From Secs. III A–III C, parametric studies have been performed to reveal the behavior of the fibrous gap under oscillating shearing. This section will apply this model to our original problem, namely, how oscillating shearing influences behavior in SAS, as shown in Fig. 1.

In the human head, the average gap height of the SAS is about 3 mm. 16 The properties of the CSF are similar to those of water, which has a dynamic viscosity of $\mu=1.0\times 10^{-3}$ Pa s, and a density of $\rho=1.0\times 10^3$ kg/m 3 . If the head suffers an oscillating shearing with $\omega=9$ Hz, this translates into a Womersley number, Wo = $\sqrt{\rho\omega h^2/\mu}=9$. The porosity of the SAS is about 0.99, and the permeability is about 3.125×10^{-10} m 2 . 13,48 Then, the Brinkman number, $\alpha=\sqrt{h^2/k_P}\approx 169$. The Young's modulus of the fibrous trabeculae $E=1\times 10^3$ Pa. 13,49 If we assume the average strain is $\epsilon=0.018$, Bingham number, Bm = $\frac{T}{\omega\mu\pi R^2}=\frac{E\epsilon}{\omega\mu}=2000$. The results for the fluid velocity, fiber displacement, shear stress and the porous resistance in this application is shown in Figs. 12(a)-12(d), respectively.

The SAS application features high values of α and Bm. Figure 12(a) shows that the maximum fluid velocity is about twice the boundary velocity. The fiber displacement shown in Fig. 12(b) indicates that the fiber oscillation magnitude in the negative direction is as high as that of the oscillating boundary. Hence, the oscillation in the gap could be stronger than the oscillation of the boundary. Figure 12(c) indicates the shear stress at the bottom could be even higher than the shear stress at the top, which means the shear stress could easily damage the brain. Finally, as α is pretty high, the velocity difference between the CSF and the trabeculae is negligible, which is the result shown in Fig. 12(d).

The structural and mechanical properties of SAS generally remain constant for an individual, whereas the magnitude of impact forces can differ greatly. To explore this variability, Fig. 13 examines the scenario where the head is subjected to an oscillating shearing impact at a lower frequency of $\omega=1\,\mathrm{Hz}$ while other parameters are maintained. This adjustment yields dimensionless numbers of

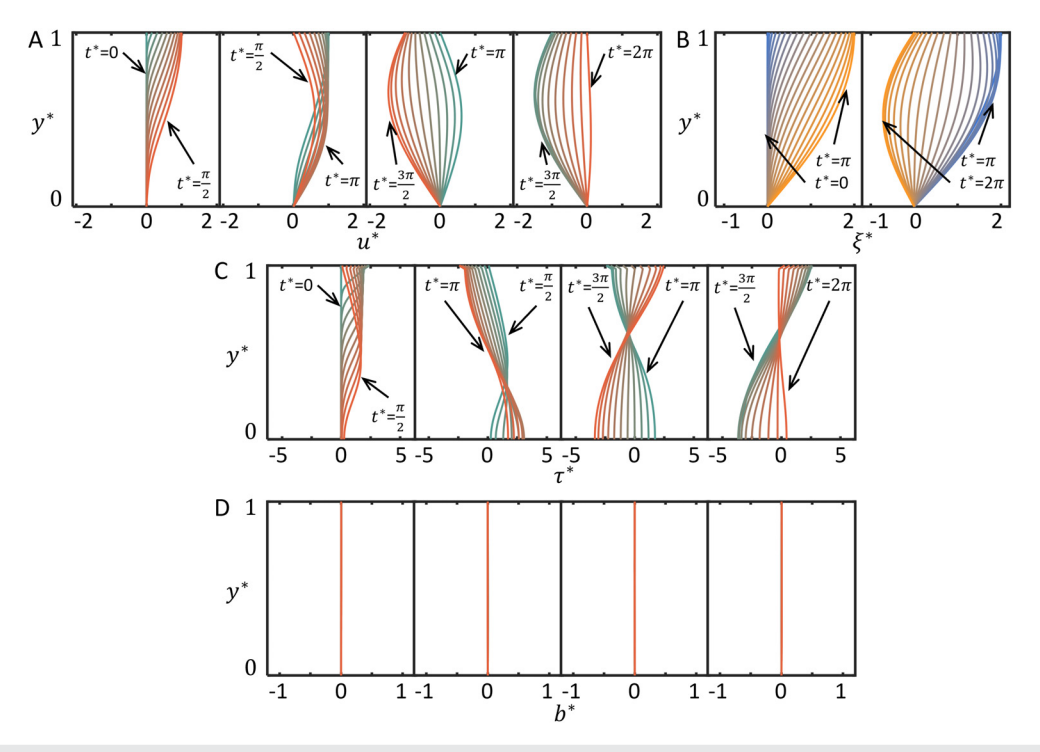


FIG. 12. (a) Fluid velocity, (b) fiber displacement, (c) shear stress, and (d) porous resistance profile across the gap for the parameters of the SAS. The results indicate the CSF velocity could be twice the oscillating boundary velocity. The trabeculae oscillation magnitude is as high as that of the boundary. Shear stress at the bottom could be higher than the shear stress at the top. The dense trabeculae tightly hold the CSF, which makes the velocity difference between the CSF and the trabeculae negligible.

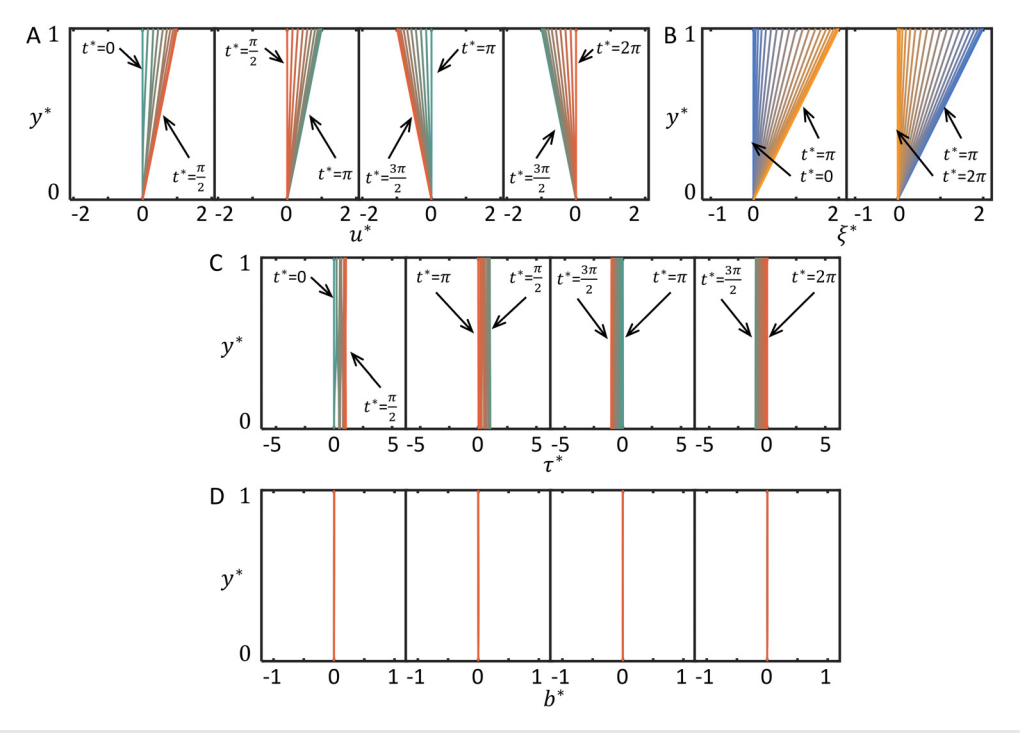


FIG. 13. (a) Fluid velocity, (b) fiber displacement, (c) shear stress, and (d) porous resistance profile across the gap for the parameters of the SAS. Lower-frequency impacts lead to reduced deformation and shear stress, potentially lowering the risk of shaking baby syndrome.

Bm = 18 000, Wo = 3, and α = 169. Figures 13(a)–13(d) display the results for fluid velocity, fiber displacement, shear stress, and porous resistance, respectively, under this condition.

The findings reveal that at a lower oscillating frequency, both fluid velocity and fiber deformation exhibit a linear behavior across the gap, and the corresponding shear stress is significantly reduced. Moreover, the difference in velocity between the fluid and the fiber remains minimal. The findings depicted in Fig. 13 indicate that the brain's response to impact is significantly affected by the frequency of the impacting force. Specifically, impacts at lower frequencies result in less severe deformation and shear stress, implying that a slower shaking impact could potentially mitigate the risk associated with shaking baby syndrome.

It is noted that the selection of parameters in this section for the calculation was guided by the balance of theoretical precision with real-world relevance. Geometric and mechanical properties were carefully chosen, reflecting data reported in the literature to anchor our model accurately in practical scenarios. The impact loading parameters were determined to represent plausible scenarios within the modeled environments. Given the variability of impact loading in real-world cases, we opted for a representative value to conduct a preliminary analysis. This approach allows us to demonstrate the model's capability while acknowledging that specific values may differ in individual cases. Our intention is to provide a foundation for further investigation and application of the model to a broad spectrum of conditions.

IV. CONCLUSION

In this paper, we have developed a novel theoretical model to examine the fluid-structure interaction of viscous fluid flow through a fibrous network driven by an oscillating boundary. The highlights of our findings are as follows:

- The primary dimensionless parameters affecting the oscillating shearing process are the Womersley number (Wo) for frequency, the Brinkman number (α) for porous structure, and the Bingham number (Bm) for fiber stiffness.
- Extensive parametric studies indicate that the oscillating frequency predominantly influences the time-dependent response of fluid velocity, fiber displacement, shear stress, and porous resistance when an oscillating motion is applied to the boundary where one end of the fibers is anchored.

We applied the model to investigate shear impact penetration from the skull through the fibrous AT in the SAS to the brain matter, aiming to gain crucial insights into force transmission mechanisms relevant to shaken baby syndrome. Our findings revealed that:

- Oscillations of CSF and AT can substantially surpass boundary oscillations.
- 2. Shear stress has the potential to penetrate the SAS, potentially reaching the brain with heightened intensity, indicating an increased risk of brain injury.

The developed theoretical model advances the understanding of fluid-structure interactions, offering critical insights into fibrous network dynamics within physiological settings. Despite its strengths, the model's assumptions, unidirectional flow, and liner fiber deformations may limit its scope. When investigating a heterogeneous fiber network, variations in flow along the flow direction occur. Under these

conditions, the current governing equations, Eqs. (1) and (4), remain applicable. However, to accurately model these variations, a numerical approach must be employed. Future research would refine these aspects to broaden the model's accuracy and applicability.

The CSF directly interacts with additional layers like the dura and pia mater, which exhibit hyperelastic behavior and offer significant damping during large deformations. However, these effects were not addressed in the current paper. Our team's ongoing work focuses on developing a dynamic response model for these layers, ensuring their deformation aligns with the existing boundary conditions. This enhancement is anticipated to enhance the current model's capability to simulate more realistic biomechanical interactions within the CSF, thereby advancing our understanding of physiological impacts under various conditions.

ACKNOWLEDGMENTS

This research was supported by the National Science Foundation under Award No. 2322067. Dr. Lang acknowledges the support from the National Natural Science Foundation of China (No. 12202101) and the Natural Science Foundation of Jiangsu Province (No. BK20220793).

AUTHOR DECLARATIONS

Conflict of Interest

The authors have no conflicts to disclose.

Author Contributions

Ji Lang: Conceptualization (equal); Methodology (lead); Writing – original draft (lead). Liyun Wang: Conceptualization (equal); Validation (equal); Writing – review & editing (supporting). Qianhong Wu: Conceptualization (equal); Project administration (lead); Writing – review & editing (lead).

DATA AVAILABILITY

The data that support the findings of this study are available from the corresponding author upon reasonable request.

NOMENCLATURE

- b porous resistance received by the fluid
- b^* dimensionless porous resistance received by the fluid
- Bm Bingham number, $T/(\omega \mu \pi R_f^2)$
 - E Young's modulus of the fibrous trabeculae
- F_l fluid drag force on the fiber
- h gap height
- K_p Darcy permeability
- M integer indicating the number of terms in the Euler algorithm
- P pressure
- R_f fiber radius
- s Laplace operator
- T tension force of the fiber
- t time
- *t** dimensionless time

- u horizontal components of the local macroscopic velocity
- u local macroscopic fluid velocity
- u' horizontal components of the microscopic velocity
- u' microscopic fluid velocity
- *u** dimensionless fluid velocity
- \bar{u} Laplace transform of u^*
- V_0 characteristic velocity
- y vertical coordinate
- *y** dimensionless vertical coordinate
- α Brinkman number, $\sqrt{h^2/K_P}$

$$\beta_1$$
 $s^2 \frac{Wo^2 \eta}{Bm} + s \left(Wo^2 + \frac{1}{Bm} \frac{\alpha^2 \phi}{1 - \phi}\right) + \alpha^2$

$$\beta_2 \qquad s^3 \frac{\mathrm{Wo}^4 \eta}{\mathrm{Bm}} + s^2 \frac{\mathrm{Wo}^2 \alpha^2}{\mathrm{Bm}} \left(\frac{\phi}{1 - \phi} + \eta \right)$$

- δ_k , γ_k , ζ_k coefficients used in the Euler algorithm, k = 0, 1, ..., M
 - $\eta \rho_s/\rho$
 - $\lambda_1 \qquad \sqrt{\frac{\beta_1 + \sqrt{\beta_1^2 4\beta_2}}{2}}$
 - $\lambda_2 \sqrt{\frac{\beta_1 \sqrt{\beta_1^2 4\beta_1}}{2}}$
 - μ dynamic viscosity
 - ξ fiber displacement
 - ξ^* dimensionless fiber displacement
 - ξ Laplace transform of ξ
 - ρ density of the fluid
 - ρ_s density of the fiber
 - τ shear stress
 - τ^* dimensionless shear stress
 - ω angular frequency
 - ϵ average strain
 - ϕ porosity

REFERENCES

- ¹H. Li, J. H. Deng, J. H. Yin, and J. B. Zhu, "Modelling the shearing behaviour of joints using an improved shear box genesis approach in particle flow code (2D) and its validation," Geomech. Geophys. Geo-Energy Geo-Resources 6, 15 (2020).
- ²H. Zhou, X. Chen, Y. Zhang, Y. Ai, and D. Sun, "An analysis on the influence of air ingestion on vibration damping properties of squeeze film dampers," Tribol. Int. 145, 106168 (2020).
- ³M. M. Mortazavi, S. A. Quadri, M. A. Khan, A. Gustin, S. S. Suriya, T. Hassanzadeh *et al.*, "Subarachnoid trabeculae: A comprehensive review of their embryology, histology, morphology, and surgical significance," World Neurosurg. 111, 279–290 (2018).
- ⁴E. Lauga and T. R. Powers, "The hydrodynamics of swimming microorganisms," Rep. Prog. Phys. **72**, 096601 (2009).
- ⁵M. J. Shelley, "The dynamics of microtubule/motor-protein assemblies in biology and physics," Annu. Rev. Fluid Mech. **48**, 487–506 (2016).
- ⁶J. Feng and S. Weinbaum, "Lubrication theory in highly compressible porous media: The mechanics of skiing, from red cells to humans," J. Fluid Mech. **422**, 281–317 (2000).
- ⁷Q. Wu, Y. Andreopoulos, and S. Weinbaum, "From red cells to snowboarding: A new concept for a train track," Phys. Rev. Lett. 93, 194501 (2004).
- ⁸T. Gacka, Z. Zhu, R. Crawford, R. Nathan, and Q. Wu, "From red cells to soft lubrication, an experimental study of lift generation inside a compressible porous layer," J. Fluid Mech. 818, 5–25 (2017).
 ⁹Z. Zhu, R. Nathan, and Q. Wu, "An experimental study of the lubrication the-
- ⁹Z. Zhu, R. Nathan, and Q. Wu, "An experimental study of the lubrication theory for highly compressible porous media, with and without lateral leakage," Tribol. Int. 127, 324–332 (2018).
- ¹⁰N. Benko, E. Luke, Y. Alsanea, and B. Coats, "Spatial distribution of human arachnoid trabeculae," J. Anat. 237, 275–284 (2020).

- ¹¹N. Benko, E. Luke, Y. Alsanea, and B. Coats, "Mechanical characterization of the human pia-arachnoid complex," J. Mech. Behav. Biomed. Mater. 120, 104579 (2021).
- ¹²S. Gupta, M. Soellinger, D. M. Grzybowski, P. Boesiger, J. Biddiscombe, D. Poulikakos *et al.*, "Cerebrospinal fluid dynamics in the human cranial subarachnoid space: An overlooked mediator of cerebral disease. I. Computational model," J. R. Soc. Interface 7, 1195–1204 (2010).
- ¹³P. Saboori, "Subarachnoid space trabeculae architecture," Clin. Anat. 34(1), 40–50 (2021).
- ¹⁴H. E. Killer, H. R. Laeng, J. Flammer, and P. Groscurth, "Architecture of arachnoid trabeculae, pillars, and septa in the subarachnoid space of the human optic nerve: Anatomy and clinical considerations," Br. J. Ophthalmol. 87, 777–781 (2003).
- ¹⁵D. G. Talbert, "That the shaken baby syndrome is based on a false subarachnoid model and is therefore invalid," OA Med. Hypothesis 2(1), 1–4 (2014).
- 16P. Saboori and A. Sadegh, "Material modeling of the head's subarachnoid space," Sci. Iran 18, 1492–1499 (2011).
- ¹⁷P. Saboori, C. Germanier, and A. Sadegh, "Mechanics of CSF flow through trabecular architecture in the brain," in 26th Southern Biomedical Engineering Conference SBEC 2010, April 30–May 2, 2010 (Springer, 2010), pp. 440–443.
- ¹⁸Centers for Disease Control and Prevention, "Sports-related recurrent brain injuries—United States," Morb. Mortal. Wkly. Rep. 46, 224–227 (1997).
- ¹⁹D. J. Thurman, C. M. Branche, and J. E. Sniezek, "The epidemiology of sports-related traumatic brain injuries in the United States: Recent developments," J. Headache Traumatol. Rehabil. 13, 1–8 (1998).
- ²⁰D. H. Janda, C. Bir, and B. Kedroske, "A comparison of standard vs. breakaway bases: An analysis of a preventative intervention for softball and baseball foot and ankle injuries," Foot Ankle Int. 22, 810–816 (2001).
- ²¹I. Blumenthal, "Shaken baby syndrome," Postgrad. Med. J. **78**(926), 732–735 (2002).
- ²²J. D. Kivlin, K. B. Simons, S. Lazoritz, and M. S. Ruttum, "Shaken baby syndrome," Ophthalmology 107, 1246–1254 (2000).
- ²³D. G. Talbert, "The embryological development of the form of the trabeculae bridging the subaracnoid space," J. Traumatol. Treat. 3, 198 (2014).
- ²⁴H. J. Obremski and A. A. Fejer, "Transition in oscillating boundary layer flows," J. Fluid Mech. **29**, 93–111 (1967).
- 25S. H. Davis, "The stability of time-periodic flows," Annu. Rev. Fluid Mech. 8, 57-74 (1976).
- ²⁶M. T. Landahl, "A note on an algebraic instability of inviscid parallel shear flows," J. Fluid Mech. 98, 243–251 (1980).
- ²⁷N. Cagney and S. Balabani, "Taylor-Couette flow of shear-thinning fluids," Phys. Fluids 31, 053102 (2019).
- ²⁸P. Ramesh, S. Bharadwaj, and M. Alam, "Suspension Taylor-Couette flow: Co-existence of stationary and travelling waves, and the characteristics of Taylor vortices and spirals," J. Fluid Mech. 870, 901–940 (2019).
- ²⁹R. Ellahi, M. H. Tariq, M. Hassan, and K. Vafai, "On boundary layer nanoferroliquid flow under the influence of low oscillating stretchable rotating disk," J. Mol. Liq. 229, 339–345 (2017).
- 30 M. R. Hassan, J. Zhang, and C. Wang, "Deformation of a ferrofluid droplet in simple shear flows under uniform magnetic fields," Phys. Fluids 30, 092002 (2018)
- ³¹M. Luhar and H. M. Nepf, "Wave-induced dynamics of flexible blades," J Fluids Struct. 61, 20–41 (2016).
- ³²P. J. Zuk, A. M. Słowicka, M. L. Ekiel-Jeżewska, and H. A. Stone, "Universal features of the shape of elastic fibres in shear flow," J. Fluid Mech. 914, A31 (2021).
- 33L. E. Becker and M. J. Shelley, "Instability of elastic filaments in shear flow yields first-normal-stress differences," Phys. Rev. Lett. 87, 198301 (2001).
- 340. Du Roure, A. Lindner, E. N. Nazockdast, and M. J. Shelley, "Dynamics of flexible fibers in viscous flows and fluids," Annu. Rev. Fluid Mech. 51, 539–572 (2019).
- 35Y. Han, S. Weinbaum, J. A. E. Spaan, and H. Vink, "Large-deformation analysis of the elastic recoil of fibre layers in a Brinkman medium with application to the endothelial glycocalyx," J. Fluid Mech. 554, 217 (2006).
- ³⁶D. Vijay Anand, B. S. V. Patnaik, and S. Vedantam, "A dissipative particle dynamics study of a flexible filament in confined shear flow," Soft Matter 13, 1472–1480 (2017).
- ³⁷Z. Zhu, R. Nathan, and Q. Wu, "Multi-scale soft porous lubrication," Tribol. Int. 137, 246–253 (2019).

- Xu, S. Weinbaum, and Y. Andreopoulos, "Stagnation-point flows in a porous medium," Chem. Eng. Sci. 60(1), 123–134 (2005).
 Lang, R. Nathan, and Q. Wu, "Theoretical and experimental study of
- ³⁹j. Lang, R. Nathan, and Q. Wu, "Theoretical and experimental study of transient squeezing flow in a highly porous film," Tribol. Int. 135, 259–268 (2019).
- 40H. P. G. Darcy, Les Fontaines Publiques de la ville de Dijon: Exposition et Application des Principes à Suivre et des Formules à Employer dans les Questions de Distribution D'eau (Victor Dalamont, 1856).
- ⁴¹H. Wu, "Squeeze-film behavior for porous annular disks," J. Lubr. Technol. 92, 593–596 (1970).
- ⁴²N. B. Naduvinamani, P. S. Hiremath, and G. Gurubasavaraj, "Squeeze film lubrication of a short porous journal bearing with couple stress fluids," Tribol. Int. 34, 739–747 (2001).
- ⁴³T. Karmakar and G. P. Raja Sekhar, "Squeeze-film flow between a flat impermeable bearing and an anisotropic porous bed," Phys. Fluids 30, 043604 (2018).

- ⁴⁴M. H. Hamdan, "Single-phase flow through porous channels a review of flow models and channel entry conditions," Appl. Math. Comput. 62, 203–222 (1994).
- 45J. Lang and Q. Wang, "Theoretical modeling of squeezing flow in porous media under arbitrary boundary velocity," Tribol. Int. 191, 109086 (2024).
- 46). Lang, L. Wang, and Q. Wu, "Theoretical study of oscillating squeezing flow through a porous medium," Tribol. Int. 162, 107110 (2021).
- ⁴⁷J. Abate and W. Whitt, "A unified framework for numerically inverting laplace transforms," INFORMS J. Comput. 18, 408–421 (2006).
- 48Y. Tada and T. Naaoshimo, "Modeling and simulation of brain lesions by the Finite-Element method," IEEE Eng. Med. Biol. Magn. 13, 497-503 (1994).
- 49P. Saboori and A. Sadegh, "On the properties of brain sub arachnoid space and biomechanics of head impacts leading to traumatic brain injury," Adv. Biomech. Appl. 1, 253–267 (2014).